

Detection of GPS C/A Code Self-Interference: Monitor Overview and Applicability

Jessica Belzer | Frank van Graas

Ohio University

Correspondence

Jessica Belzer
Avionics Engineering Center
Stocker Center 210
Ohio University
Athens, OH 45701-2979
Email: jb269209@ohio.edu

Abstract

Self-interference can cause large errors of up to tens of meters on the GPS C/A code pseudorange measurement. Although the probability of an occurrence of large self-interference errors is small, to enable the use of C/A code phase measurements in high accuracy or safety-of-life applications, a detection or mitigation method is needed. A stressful case of self-interference is modeled on a GPS hardware simulator to investigate monitor performance using real signal results. A summary of contributions in this paper follows. Self-interference pseudorange error characteristics within and mitigation requirements for the Ground Based Augmentation System (GBAS) Approach Service Type D (GAST-D) environment are identified. Existing monitors are evaluated for their response to self-interference and their ability to detect the error based on the GAST-D environment. This includes the potential for misidentification of the error. A novel Frequency Domain Cross-Correlation (FDCC) detector is proposed that can uniquely identify self-interference error with no siting constraints.

Keywords

GBAS, GPS cross correlation, GPS self-interference, ground based augmentation system

1 | INTRODUCTION

Self-interference error on the GPS C/A code pseudorange measurement was first identified in Spilker (1978). It was determined to cause error on the order of tens of meters in van Nee (1992). Van Dierendonck et al. (2002) demonstrated that cross-correlation error can be modeled in a laboratory setting for investigation. Although the error is rare, Doppler crossover events can cause sustained error on the pseudorange measurement. This presents a challenge for safety-of-life applications such as the Ground Based Augmentation System (GBAS), used in commercial aircraft runway approach and landing.

Self-interference occurs when two C/A codes cross-correlate, and the Doppler frequency offset between the signals causes their spectral lines to overlap. When a receiver tracks a signal experiencing self-interference, energy from the interfering satellite leaks into the tracking results. The autocorrelation peak becomes a sum of the autocorrelation and the cross-correlation energy. Distortion to the peak translates to tracking and pseudorange error.

Doppler crossover events were observed to occur at a rate of 0.22 pairs of satellites per minute over a 24-hour period (Zhu & van Graas, 2005). During each crossover, self-interference may or may not occur. The Doppler crossovers were observed by a stationary user (Zhu & van Graas, 2005) similar to a ground reference receiver used in a GBAS.

GBAS provides differential GPS corrections to mitigate errors shared by the receiver aboard an approaching aircraft and the reference receivers located near the runway (FAA, n.d.). Error caused by self-interference is generally not common to both locations (Zhu & van Graas, 2014), and primarily affects the ground receivers. Current GBAS Approach Service Type C (GAST-C) operations enable aircraft approaches down to Category I weather minima (FAA, n.d.).

Zhu and van Graas (2014) provide an overview of L1 C/A code self-interference within the context of GBAS. This includes error on the pseudorange measurement for a Doppler crossover event. Most of the C/A code self-interference error dependencies are known such that the error can be simulated. However, atmospheric signal delays cause cross-correlation error between two satellites to be partially randomized in terms of the time and location where a self-interference event will occur.

While the error is considered deterministic for modeling purposes, some of the dependencies may be difficult to predict (Zhu & van Graas, 2005). Self-interference errors are a function of the time constant used to smooth the code with the carrier-phase measurements, receiver correlator spacing, signal integration time, and relative received signal strengths of the affected satellites. The error also depends on the tracking loop filtering, relative C/A code offset, Doppler frequency difference between the signals, the navigation data bits and data bit offset, and the relative phase (Zhu & van Graas, 2005, 2014). Two satellites affected by C/A code self-interference may transmit different downlink data. The error effects caused by self-interference depend on the relative navigation data bit values transmitted. An upper bound on the maximum self-interference error for an unsmoothed pseudorange measurement is presented in Zhu and van Graas (2014).

In Van Dierendonck et al. (2002), the authors demonstrate a mitigation strategy of smoothing the code with the carrier-phase measurements using a Hatch filter with a 100-s smoothing time constant (Hatch, 1982; Van Dierendonck et al., 2002). GAST-C smooths the pseudorange measurement in this way (RTCA SC-159, 2017). In addition, self-interference is mitigated based on a table of screening conditions (Zhu & van Graas, 2011). The pseudorange error is bound by the sigma pseudorange ground broadcast parameter (Zhu & van Graas, 2011).

GBAS Approach Service Type D (GAST-D) service will enable GBAS approaches down to Category III weather minima up to a touchdown on the runway. To certify GAST-D operations, the self-interference mitigation solution must be revisited to ensure it meets increased integrity requirements. The requirements include a pseudorange smoothing time constant of 30 s. The pseudorange error bound of 1.6 m has a probability of occurrence of 10^{-9} per approach, and an error that exceeds the pseudorange error bound must be detected within a 2-s time to alert (ICAO NSP/3, 2016). Since the error is considered deterministic in that it can be modeled (Van Dierendonck et al., 2002; Zhu & van Graas, 2014), it should be detected or mitigated. The solution for GAST-D must also be robust to self-interference caused by ghost satellites or increased power differentials from flex power (Steigenberger et al., 2019). A ghost satellite is a satellite that is not tracked by the receiver. Examples of ghost satellites are active satellites that are set unhealthy or satellites that are not in the almanac (Belzer & van Graas, 2019). Flex power has the potential to significantly increase self-interference errors through increased received power differentials between satellites. These two factors were not considered for GAST-C.

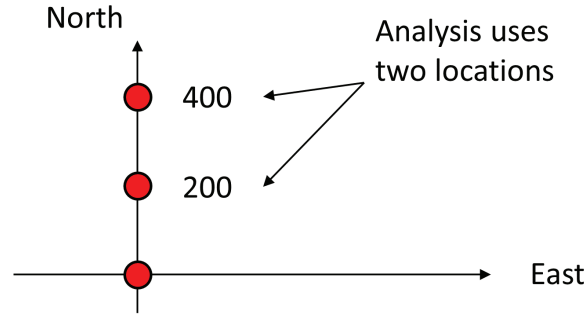


FIGURE 1 Observation locations used in simulator experiment

Many previously proposed mitigation methods require tracking the interfering GPS C/A code signals and are not applicable to ghost satellites. An exception to this is the Signal Deformation Monitor (SDM). The SDM is primarily used in GBAS to detect satellite hardware faults that affect the transmitted C/A code waveform (Houston et al., 2011). In their 2011 paper, Houston et al. investigated the applicability of the SDM to detecting self-interference in the GBAS GAST-D environment. It was found that the SDM in combination with the Code-Carrier Divergence (CCD) monitor was able to detect self-interference error on the pseudorange measurement (Houston et al., 2011). However, significant modifications to the monitor would be required to apply the SDM to detect self-interference in the GAST-D environment. The detector would not only need to detect self-interference, it would also need to be able to distinguish this interference from a true SDM fault. Otherwise, self-interference could cause the removal of the satellite for an extended period of time, since SDM faults are satellite based. The SDM was not selected for further study in this research.

Another option considered in this research was to design a receiver that acquires and tracks all possible C/A codes. This capability would ensure that all satellites that can cause C/A code self-interference are tracked by the receiver. Self-interference error could then be monitored based on the approach used in GAST-C. This option would require a significant redesign of the receiver used in the ground station. As a result, the option was not selected for further study in this research.

This paper evaluates four monitors for their ability to detect self-interference with a focus on meeting GAST-D requirements. Monitors are evaluated using a GPS hardware simulation of a stressful self-interference event. The geometry of the event is such that the self-interference conditions last for a period greater than 12 seconds. Three GBAS monitors are investigated: the Code-Carrier Divergence (CCD) monitor, the Dual Solution Ionospheric Gradient Monitoring Algorithm (DSIGMA), and the Bias-Value (B-Value) monitor. A novel Frequency Domain Cross-Correlation (FDCC) detector is also presented. The FDCC detector is the first frequency-based self-interference detection method. This approach allows for early detection and does not impose siting constraints on the reference receivers.

The CCD monitor, DSIGMA, and B-Value monitor were evaluated in previous work (Belzer & van Graas, 2019). The results are summarized. The B-Value monitor is demonstrated using two locations, shown in Figure 1. The remainder of the monitors use the 200-m north location. All plots are referenced to the same start GPS time of week, 20990.895 s.

The CCD monitor is defined in RTCA SC-159 (2017). It is applied for the detection of satellite signal generation faults and ionospheric gradients and consists of the following set of equations:

$$D_n = (1 - k)D_{n-1} + k \cdot Z_n \quad (1)$$

$$Z_n = (1 - k)Z_{n-1} + k \cdot dz_n \quad (2)$$

In Equations (1) and (2), D_n is the filtered value, and Z_n is a filter state. n describes the current epoch number of the filter. k describes a weighting parameter. It equals the length of the epoch divided by 100 seconds. Equation (3) plays a role in evaluating the filter state:

$$dz_n = \frac{\left[\rho_n - \left(\frac{\lambda}{2\pi} \right) \phi_n \right] - \left[\rho_{n-1} - \left(\frac{\lambda}{2\pi} \right) \phi_{n-1} \right]}{t_n - t_{n-1}} \quad (3)$$

In this expression, λ is the wavelength of the L1 carrier in meters, ρ is the raw pseudorange measurement in meters, and ϕ represents the accumulated carrier phase in radians. t represents the time in seconds. The CCD monitor flags a satellite either when the magnitude of the monitor value is greater than 0.0415 m/s, or when the monitor value fails to be resolved for more than 30 s during the monitor history window (RTCA SC-159, 2017).

The CCD monitor showed a response to the self-interference event (Belzer & van Graas, 2019). It was evaluated using 30-s and 100-s smoothing time constants. However, the smoothing inherent to the filter means that reliable detection within the time to alert is a concern. The point where the monitor may exceed the threshold may not correspond to the point of the error's worst severity. The monitor was not recommended for further investigation (Belzer & van Graas, 2019).

The DSIGMA is also presented in RTCA SC-159 (2017) and is applied to monitor the effects of the ionosphere. The monitor value is given by Equation (4; RTCA SC-159, 2017):

$$P_{diff} = \rho_{corr,100} - \rho_{corr,30} \quad (4)$$

where ρ stands for the current corrected pseudorange measurements that have been smoothed with the carrier phase using 100 s and 30 s time constants. A satellite is flagged when the monitor value, P_{diff} , exceeds 0.976 meters (RTCA SC-159, 2017). The DSIGMA responded to the event on the weak satellite signal but did not exceed the threshold. Due to the inconsistent response and inherent smoothing, the DSIGMA was also excluded from further investigation (Belzer & van Graas, 2019). Additional perspective on the CCD monitor and DSIGMA results is given in this paper.

The B-Value monitor uses multiple reference receivers. The monitor equation is given in Dautermann et al. (2011) and RTCA SC-159 (2008), reproduced in Equation (5; Dautermann et al., 2011). Its purpose is to detect excessive reference receiver measurement errors (Dautermann et al., 2011). The monitor operates by comparing the broadcast pseudorange correction for a given satellite (i) minus the mean of the corrections generated at a subset of receivers (excluding a chosen receiver, j):

$$B(i, j) = PRC_{TX}(i) - \frac{1}{M(i) - 1} \sum_{k \neq j} PRC_{SCA}(i, k) \quad (5)$$

PRC_{TX} is the broadcast pseudorange correction for the satellite generated by the ground station. M is the number of receivers used to compute the correction for satellite i . All pseudorange corrections include smooth clock adjustments (SCAs) applied to the results from each receiver, and k represents the receiver index such

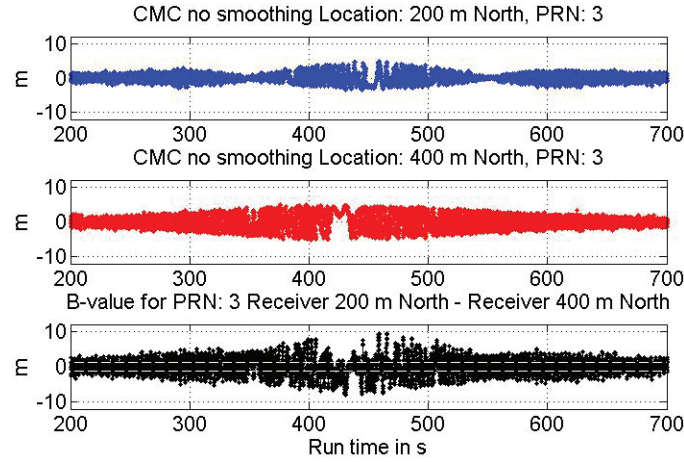


FIGURE 2 Code minus carrier measurements and bias value without smoothing for PRN 3

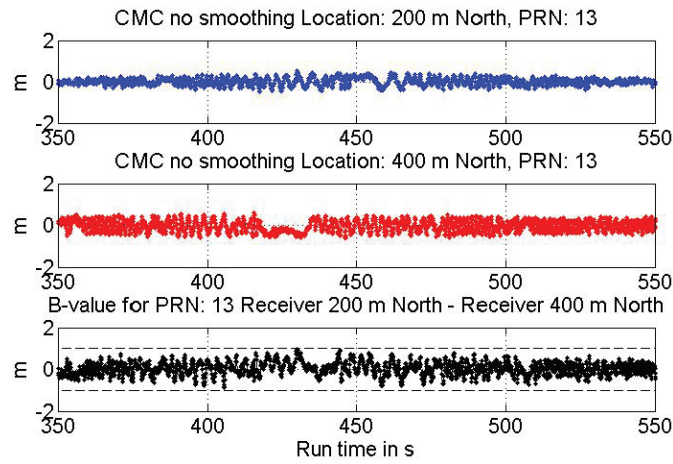


FIGURE 3 Code-minus-carrier measurements and bias value without smoothing for PRN 13

that the B-Value receiver (j) is excluded (Dautermann et al., 2011; RTCA SC-159, 2008).

The B-Value monitor is demonstrated using two locations. The locations are offset in 200-m increments from the stressful self-interference event observation point. Code-minus-carrier (CMC) measurements are used to approximate the pseudorange corrections. No ionospheric effects are included in the event.

In the two-receiver case, the monitor reduces to the pseudorange correction at one location minus the pseudorange correction at the other. An approximate threshold is derived in this paper. The threshold is marked in Figure 2 and Figure 3 but further discussed in the Bias-Value monitor section. In Belzer and van Graas (2019), the B-Value monitor was evaluated using unsmoothed CMC measurements. The monitor fully imaged the error on the pseudorange measurement. The error was observable because the Doppler difference between the affected satellites is different when observed at each location; the Doppler crossover occurs at different times. The latter is key for the ability of the B-Value monitor to detect self-interference.

The error on the pseudorange measurement is frequency modulated by the Doppler difference between the affected satellites. Therefore, the frequency modulation never fully cancels when the measurements are subtracted. This can be observed in Figure 2 and Figure 3. The Doppler crossover event is observable in the

CMC results as the point where the frequency modulation of the error approaches 0 Hz. Overall, the monitor response is strong and offers potential as a solution to detect the error (Belzer & van Graas, 2019). The monitor exceeds the threshold for the weak satellite, PRN 3, but not for the strong satellite, PRN 13. The B-Value monitor is further investigated in this paper.

Based on its current implementation in GAST-C, the B-Value monitor uses smoothed measurements. The smoothed-measurement approach is investigated in this paper. The minimum number of receivers required to operate the monitor is also resolved. Theory and methods for evaluation of the B-Value monitor and the FDCC detector using the simulated stressful case self-interference experiment follow.

2 | THEORY AND METHODS

2.1 | Simulator Experiment

A GPS hardware simulation of a stressful case of self-interference consisting of a Doppler crossover event was used in this research (Belzer & van Graas, 2019). The self-interference occurs between PRN 13 and 3, with a 10-dB received power differential. A 10-dB power difference was selected due to the receiver antenna pattern and differences in satellite transmit power. The event is a stressful case based on the satellite geometry using the optimized 24-satellite constellation used for testing (RTCA SC-159, 2008, 2017). Due to the satellite geometry, the cross-correlation conditions last for a duration greater than 12 s. The event was selected to simulate the period of 12 s where the two navigation data almanac subframes on both C/A code signals in a self-interfering pair could match.

The observation location of the event is latitude 25 degrees south, and longitude 2 degrees east. This describes the origin point in Figure 1. The size of the self-interference error could be further increased if the power differential is larger than 10 dB due to, for example, flex power. The relative code offset between the PRN was set to create maximum cross-correlation between the C/A codes. This was achieved by adjusting the satellite clock offset in the simulator. Atmospheric effects were excluded from the simulations, making the error deterministic (Zhu & van Graas, 2005).

The expected tracking error from the simulated event was determined using the error envelope equation presented by Zhu and van Graas (2014) given in Equation (6).

$$e_{max} = 293d10^{\left(\frac{\gamma-23.9}{20}\right)} m \quad (6)$$

The pseudorange error in meters depends on the correlator spacing in chips, d , and the relative signal strength in dB, γ (Zhu & van Graas, 2014). A correlator spacing of 0.1 chips was used to reflect the characteristics of a GBAS ground reference receiver. Based on Equation (6), the expected pseudorange errors are 5.91 m on the weak satellite, and 0.59 m on the strong satellite. These correspond to PRN 3 and 13, respectively. Previously, in stressful cases of Doppler crossover events, it was assumed that only the weak satellite would experience significant error (Zhu & van Graas, 2005). To mitigate self-interference in the modern environment of flex power and ghost satellites, both signals should be monitored and removed from the broadcast if the pseudorange error builds to the bound.

The self-interference event consists of a Doppler crossover where the difference between the frequencies is within 0.1 Hz for 18 s. Both affected satellites have elevation angles above 50 degrees. The event was simulated on a Spirent 4760 GPS hardware simulator using a 24-satellite constellation (RTCA SC-159, 2008, 2017). Data was collected at intermediate frequency (IF) in a 20-MHz bandwidth using a universal software radio peripheral (USRP) software-defined radio (SDR). The simulator and the USRP were frequency synchronized using an external Rubidium oscillator. The data was processed for two locations, 200-m and 400-m north of the stressful case origin.

Signals were processed using two SDRs: the ChameleonChips Software-Defined Radio Toolbox (Gunawardena, 2013), and a batch processing SDR (Soloviev et al., 2005). The results for the CCD monitor, DSIGMA, and B-Value monitor were formed using the ChameleonChips SDR Toolbox. This was also used to generate the smoothed pseudorange measurement results. A 1/12-chip correlator spacing was used.

A batch processing based SDR software (Soloviev et al., 2005) was used to implement the FDCC detector. This software offers full control of the receiver tracking loop configurations, and a high update rate measurement output of 20 ms (50 Hz). An update rate of 50 Hz was selected based on the navigation data rate. The C/A code signal navigation data is transmitted at 50 bps. Based on this, it is considered possible that nominal C/A code signal tracking could be performed using coherent integration periods up to 20 ms (to decode the navigation data), and measurements could in theory be output at this rate for a GBAS receiver.

Batch estimation of the signal parameters creates independent measurements at each epoch, simplifying statistical techniques. In these results, a 0.4-chip correlator spacing was used. A wider correlator spacing was selected to amplify the cross-correlation error to make the error more observable by the FDCC detector.

2.2 | Bias-Value Monitor

The B-Value monitor compares the pseudorange corrections formed for a satellite with the mean of the pseudorange corrections formed for that satellite at all but one reference receiver location. The monitor value is given by Equation (5) in Section 1 (Dautermann et al., 2011; RTCA SC-159, 2008). Two reference receiver locations depicted in Figure 1 were used to screen the simulated self-interference event described in Section 2.1 using the B-Value monitor. As demonstrated, the monitor equation simplifies to a simple subtraction. In previous work, the B-Value monitor was found to have the potential to detect self-interference using unsmoothed pseudorange measurements (Belzer & van Graas, 2019). In practice, for the GAST-D environment, 30-s smoothed pseudorange measurements would be used. This paper investigates the 30-s smoothed pseudorange B-Value response.

While the monitor is demonstrated using two receivers, it could use more than two receiver locations. The B-Value monitor images self-interference through geometry where the Doppler projections of the affected satellites differ based on the observation location. This causes the responses at each location to differ such that subtraction does not cancel the error.

As demonstrated, the monitor could experience a blind spot to self-interference if two receiver locations are used. A blind spot would occur if there exists a geometry (satellite and receiver combination) where the error is hidden. A software simulation was used to investigate whether a blind spot exists for a monitor configuration

using two receivers. If a blind spot occurs, a significant amount of error would cancel between the pseudorange measurements at both receivers. This would be true if the Doppler crossover were to happen at the same time when observed by both locations.

A 200-m separation is used in the simulation, consistent with the spacing in the simulator experiment. One receiver is held stationary at the stressful case of self-interference event origin location. A second receiver is located 200-m east and is rotated counterclockwise in 1-deg increments for a full circle around the stationary receiver. At each configuration, the self-interference event is observed, and the time of Doppler crossover is noted. The Doppler crossover times at both locations are then compared.

2.3 | Frequency Domain Cross-Correlation Detector

The FDCC detector aims to image the error on the pseudorange using two contrasting forms of signal processing. The monitor is built to detect self-interference on the pseudorange measurement based on the error's characteristic frequency modulation. Self-interference error on the pseudorange measurement is considered to have an approximately sinusoidal error shape (like multipath). Based on the characteristics of multipath presented in Braasch (1996), in cases of strong self-interference, the error will have a non-zero mean (Braasch, 1996). However, under these conditions, it is expected that the error will still have a dominant frequency modulation.

To demonstrate the feasibility of the monitor, high update rate 20-ms-epoch measurements are used. The measurements are averaged over an extended period to form a second measurement at 2-s epochs. A high-frequency sinusoidal error will cancel when averaged over the extended period but will be observable in the high update rate output. The monitor operates on the difference between the outputs when self-interference is present. The monitor equation follows in Equation (7).

$$x_{Monitor}(t) = PR\ Error_{T\ Nominal} - PR\ Error_{T\ AVG} \quad (7)$$

The FDCC monitor signal is the high update rate pseudorange measurement minus the extended average pseudorange. The monitor isolates the time-varying error, allowing self-interference to be identified and observed as a sinusoid in Gaussian noise.

The signal is screened for self-interference at each extended processing epoch. Screening is performed in the frequency domain. Methods for detecting the sinusoid in Gaussian noise are inspired by Groth (1975). Development of the hypothesis tests is based on Brown and Chin (1997). The error is detected by performing hypothesis tests using a test statistic, T , based on a discrete Fourier transform (DFT) of the monitor signal. Derivation of the test statistic and hypothesis tests follow.

The monitor signal in the frequency domain is given in Equation (8).

$$X_{Monitor}(f) = DFT(x_{monitor}(t)) \quad \text{over } T_{AVG} \quad (8)$$

Each bin of the one-sided DFT contains real and imaginary parts. The test statistic (generated for each bin) is the sum of the squared real and imaginary parts and is described in Equation (9).

$$T = (Re(X_{monitor}(f)))^2 + (Im(X_{monitor}(f)))^2 \quad (9)$$

The real and imaginary parts of the DFT for each frequency bin are normally distributed each with unit variance. T is a chi-square distributed random variable with two degrees of freedom (DOF). In general, a chi-square distributed random variable x is given by Equation (10; Brown & Chin, 1997):

$$x = \sum_{i=1}^k x_i^2 \quad (10)$$

where each x_i is a normally distributed random variable, and all have identical variance. If a random variable (or variables) x_i have a non-zero mean, x becomes non-central chi-square distributed with non-centrality parameter, λ , given by Equation (11):

$$\lambda = \sum_{i=1}^k \mu_i^2 \quad (11)$$

where μ_i is the mean of each normally distributed random variable (Brown & Chin, 1997; Vidakovic, 2011). A summary of the derivation of the test statistic and its distribution follows.

Groth (1975) proposes the detection of a sinusoid in Gaussian noise based on the DFT. Detection is based on a hypothesis test where H_0 indicates the case where only Gaussian noise is present and H_1 indicates a sinusoidal signal plus Gaussian noise is present. Under H_0 , the DFT yields the following result (Groth, 1975):

$$a'_m + ib'_m = \sum_j x_j e^{2\pi i j m / N} \quad (12)$$

In Equation (12), the left side indicates the output of the DFT, where a' and b' are the real and imaginary parts of the output for a single frequency bin, m . The right side describes the formation of the output. x_j indicates a selection of uniformly sampled data in the time domain where $j = 0, 1, \dots, N-1$ (Groth, 1975). The one-sided DFT is used in the detector to maintain independence in the results.

A power spectrum approximation for a given bin frequency is given by the test statistic. In Equation (9), the real and imaginary terms are representative of a'_m and b'_m . The terms are independent and identically Gaussian with $\mu = 0$ and $\sigma^2 = 1$. Unity variance is a departure from Groth's (1975) approach. Groth describes the test statistic for a single bin by Equation (13):

$$P'_m = (a'_m)^2 + (b'_m)^2 \quad (13)$$

When the null hypothesis is false, the power spectrum approximation contains energy from the sinusoid and the noise. The DFT yields an additional set of terms pertaining to the sinusoid, given in Equation (14; Groth, 1975):

$$c_m + id_m = \sum_j y_j e^{2\pi i j m / N} \quad (14)$$

where c and d are the real and imaginary parts of the DFT output resulting from only the sinusoid. The power spectrum approximation for a given bin is given by (Groth, 1975):

$$P_m = a_m^2 + b_m^2 \quad (15)$$

In Equation (15), the test statistic, P_m , equals the squared sums of the real and imaginary parts due to noise and the sinusoid: $a_m = a'_m + c_m$ and $b_m = b'_m + d_m$. Groth defines the distributions of the test statistic over a sum of n bins.

The total power over n bins is given by Equation (16; Groth, 1975):

$$P = \sum_m P_m \quad (16)$$

The total sinusoid power is given by Equation (17; Groth, 1975):

$$P_S = \sum_m (c_m^2 + d_m^2) \quad (17)$$

Groth presents the probability distribution function (PDF) of the test statistic as Equation (18; Groth, 1975):

$$p_n(P; P_S) = \left(\frac{P}{P_S}\right)^{(n-1)/2} e^{-(P+P_S)} I_{n-1}\left(2\sqrt{PP_S}\right) \quad (18)$$

where I signifies the modified Bessel function of the first kind. Under the alternative hypothesis, the test statistic, P , has a non-central chi-square distribution with $2n$ degrees of freedom and non-centrality parameter λ .

When the null hypothesis is true, $P_S = 0$ and the probability distribution simplifies to Equation (19; Groth, 1975):

$$p_n(P; 0) = \frac{P^{n-1}}{(n-1)!} e^{-P} \quad (19)$$

This describes a central chi-square distribution PDF with $2n$ degrees of freedom (Groth, 1975).

For each frequency bin of the one-sided DFT output, the test statistic, T , is chi-square distributed with $\text{DOF} = 2$. To achieve unit variance of the real and imaginary parts of the DFT output, signal samples are normalized by two parameters. First, samples are normalized by the standard deviation of the nominal code noise (Brown & Chin, 1997). Second, samples are normalized by the square root of a DFT scaling factor, $(NDFT/2)$, based on the implementation of the DFT in MATLAB® (MathWorks, n.d.). A one-half selection of the two-sided DFT output is used. The scaling factors ensure unity variance of the real and imaginary parts of $X_{\text{Monitor}}(f)$ for each frequency bin under H_0 .

The FDCC detector is designed to ensure a $P_{\text{FD}} = 10^{-7}$ and $P_{\text{MD}} = 10^{-9}$. These are nominal probabilities, respectively, of false detection and missed detection of excessive self-interference on the pseudorange measurement during a GAST-D approach. The exact values of these probabilities depend on the allocations of all detectors that are part of the ground station design.

The detection threshold is calculated to satisfy P_{FD} for 50 tests on the DFT frequency bins, resulting in a false detection allocation of $P_{\text{FD}}/50$ for each test. Given the null hypothesis is true, the test statistic is chi-square distributed. The threshold indicates the test statistic value for which the area under the PDF and right of the threshold equals $P_{\text{FD}}/50$.

Next, the largest test statistic out of the 50 tests is used to detect a sinusoid. If a sinusoid is present, the test statistic will have a non-central chi-square distribution with $\text{DOF} = 2$ and non-centrality parameter given by Equation (20):

$$\lambda = \left(\frac{NDFT}{2} A_n\right)^2 \quad (20)$$

where λ is the non-centrality parameter for the distribution, $NDFT$ is the number of points used in the DFT (equal to the signal length), and A_n is the sinusoid amplitude in the normalized samples. To determine the minimum required

amplitude of the sinusoid to satisfy P_{MD} , the non-centrality parameter is calculated such that the area under the PDF and left of the threshold equals the P_{MD} required of the detector. When a chi-square random variable becomes biased, the area under its PDF shifts right based on the means of the normal random variables (x_i in Equation [10]; Brown & Chin, 1997; Papoulis, 1965).

The non-centrality parameter required defines the minimum detectable sinusoid amplitude. This is given by Equation (21):

$$A_{i,min} = \sqrt{\lambda_m} \frac{\sigma_i}{\sqrt{NDFT/2}} \quad (21)$$

where $A_{i,min}$ is the minimum detectable amplitude in the measurement domain (not normalized), and σ_i is the standard deviation of the nominal code noise. The test statistic value corresponding to the minimum detectable amplitude acts as a threshold for accepting a positive self-interference detection. The acceptance threshold is calculated based on $A_{i,min}$, but the reported minimum detectable sinusoid amplitude is $2A_{i,min}$. This conservative value accounts for the case where the sinusoid frequency is between two bins. The FDCC detector threshold and minimum required non-centrality parameter are calculated once based on the monitor sampling rate and the extended processing epoch length. Since the input to the FDCC detector is normalized, the only calculation that needs to be redone is Equation (21) if the input noise changes.

3 | FDCC DETECTOR GENERATION AND SIGNAL SCREENING

The FDCC detector's frequency-based approach allows for early screening. The signal is screened over each extended processing epoch. Isolating the error using signal processing allows the FDCC monitor to be applied using a single receiver. The monitor signal is expected to highlight the frequency content of the error, allowing for earlier detection than a bias-based error detection approach. A 2-s extended averaging epoch was selected to demonstrate the feasibility of the monitor. Depending on the overall ground station design, longer averaging epochs could be used.

3.1 | Detector Generation

To verify the threshold and the minimum required sinusoid amplitude for the FDCC detector, two simulations were performed using design probabilities of $P_{FD} = 10^{-7}$ and $P_{MD} = 10^{-9}$, and a monitor sampling rate of 50 Hz. The extended averaging epoch was 2 s, and the number of points used in the DFTs was equal to the length of the input signal. 10,000 and 100,000 Monte-Carlo trials were used to generate the data displayed in the histograms for H_0 and H_1 , respectively. The histograms approximate the test statistic's PDF and are displayed to illustrate the detection threshold and the required detection probabilities.

Under H_0 , T contains only Gaussian noise. The test statistic has $DOF = 2$ and $\lambda = 0$. 50 tests are used: one for each frequency bin. The results from the Monte-Carlo trials and the marked threshold based on the theoretical distribution are shown in Figure 4. In Figure 4, most of the distribution from this simulation is left of the detection threshold, and the left vertical scale applies.

The inverse chi-square distribution yields the threshold value where the area under the theoretical PDF of this distribution and right of the threshold equals the desired P_{FD} . The threshold test statistic equals 40.060. If the maximum test statistic

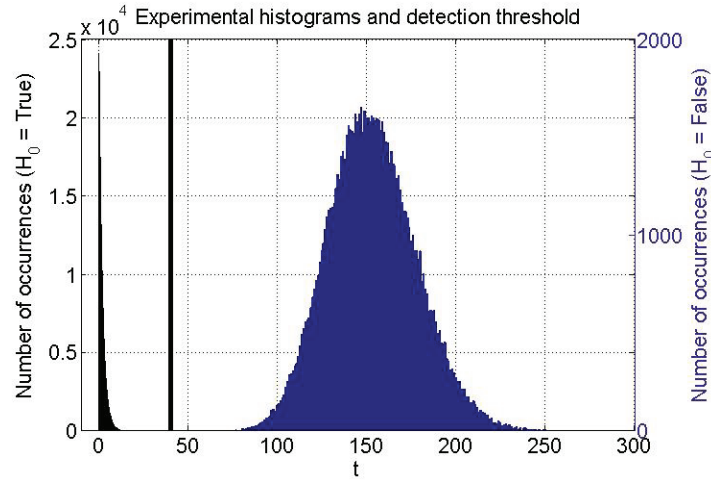


FIGURE 4 FDCC detector test statistic and threshold under H_0 (left distribution) and under H_1 (right distribution)

in the spectrum approximation over the screening epoch exceeds the threshold, self-interference is detected.

Under H_1 , the chi-square PDF of T is shifted right by the non-centrality parameter. The minimum required non-centrality is calculated such that the area under the PDF and left of the threshold equals the required P_{MD} . The results of the Monte-Carlo data from this simulation are also shown in Figure 4. The distribution from this simulation is mostly right of the detection threshold and the right vertical scale applies.

The non-centrality parameter is used to calculate the minimum detectable sinusoid amplitude. The non-centrality parameter was calculated as 150.798. The minimum detectable sinusoid amplitude in the measurement domain is given by Equation (21) and depends on the code noise.

3.2 | Signal Screening

This section presents the results of screening the signals affected by the self-interference event using the FDCC detector. The Doppler crossover event occurs between a pair of satellites: PRN 13 and 3. Both signals are screened to view the monitor response to strong and weak self-interference. PRN 13 is expected to show smaller pseudorange error as the target signal has a higher received power than the interfering signal. PRN 3 is expected to show larger pseudorange error because this target signal is weaker than the interfering signal. A summary of the self-interference event parameters is given in Table 1. Signal screening results are presented for both satellites over the same period because, when viewed from a single receiver, the frequency modulation of the error on both signals is the same. 30-s smoothed-pseudorange measurements are presented to show the monitor response versus the error pattern.

3.2.1 | Weak Satellite

A snapshot of the monitor signal for PRN 3 over 5 s is depicted in Figure 5. Given that the weak satellite is strongly affected by the self-interference event, the

TABLE 1
Self-Interference Event Parameters

Satellite (C/A code)	PRN 13	PRN 3
Relative signal strength	+10 dB	-10 dB
Maximum theoretical pseudorange error	0.59 m	5.91 m

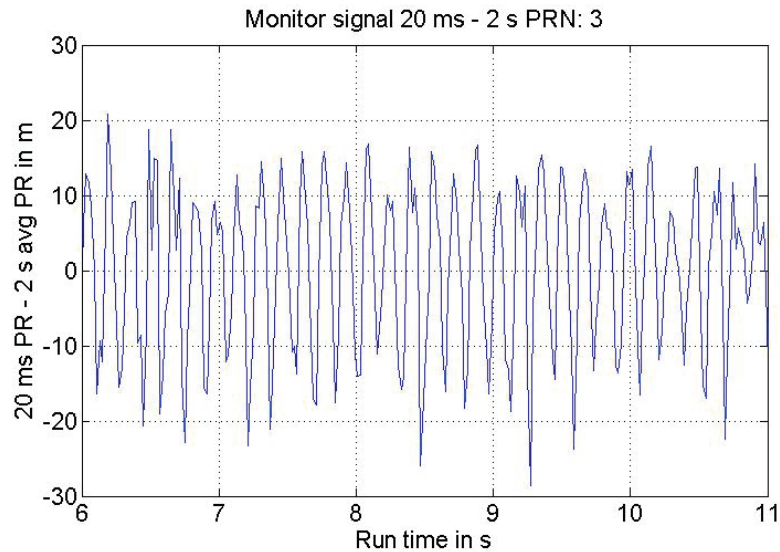


FIGURE 5 FDCC monitor signal for PRN 3

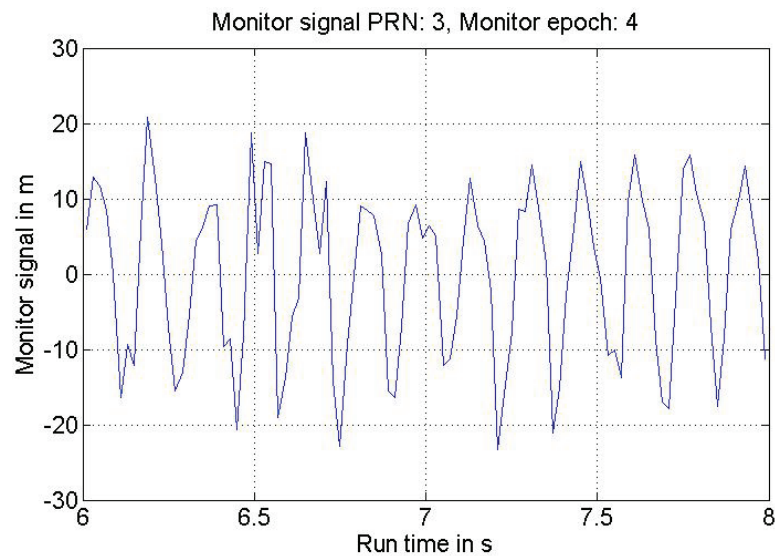


FIGURE 6 FDCC monitor signal for PRN 3 over epoch 4

sinusoidal behavior of the error is apparent. Signal screening results are presented starting with monitor epoch 4 (6-s into processing).

Figure 6 shows the monitor signal selection in the time domain used for screening. The signal has not been normalized for variance. Once the monitor signal is adjusted for variance, the DFT is performed, the test statistic calculated, and the spectral approximation is plotted.

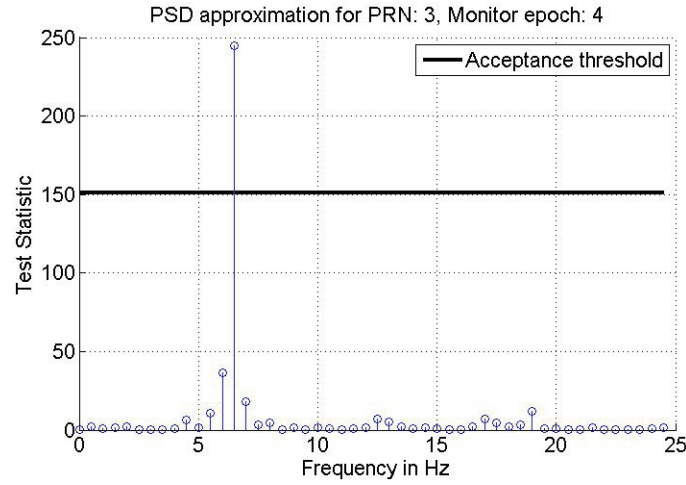


FIGURE 7 FDCC monitor signal spectrum for PRN 3 over epoch 4

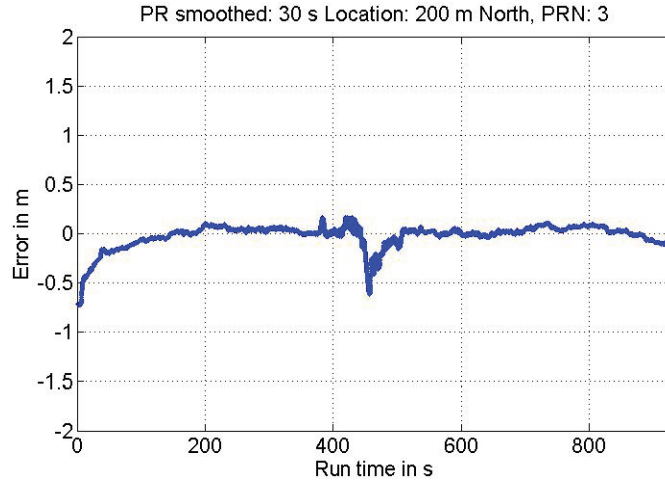


FIGURE 8 30-s smoothed CMC for PRN 3 over the duration of simulated event

A frequency of 6.5 Hz was detected in the monitor signal over the epoch shown in Figure 7. The maximum test statistic value in the spectrum exceeds the detection threshold.

To contextualize the results of the FDCC detector, the 30-s smoothed pseudorange errors were formed over the entire simulated event. These are shown in Figure 8 and Figure 12. The smoothed pseudorange errors were formed using ChameleonChips SDR Toolbox to best approximate GBAS processing. Due to software settings, the correlator spacing was set at 0.083 chips, which results in self-interference errors that are approximately 83% of those experienced by a 0.1-chip correlator spacing.

The FDCC monitor signal and monitor epoch shown take place over a runtime of 6–11 and 6–8 seconds, respectively. The worst error in the smoothed pseudorange resulting from the Doppler crossover occurs at approximately 456.5 seconds. For this signal, the C/A code noise had $\sigma_{\text{code}} = 5.658$, and conservative minimum detectable sinusoid amplitude $2A_{i,\min} = 19.653$ m. The minimum detectable sinusoid amplitude corresponds to unsmoothed pseudorange measurements. Once smoothed, the self-interference error magnitude is significantly reduced as shown in Figure 8.

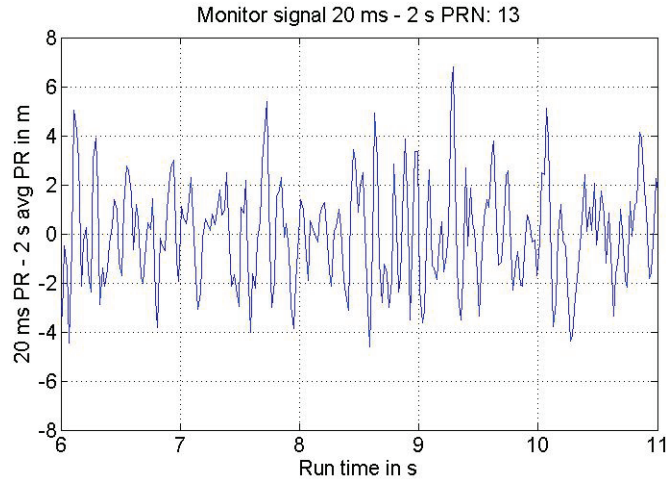


FIGURE 9 FDCC monitor signal for PRN 13

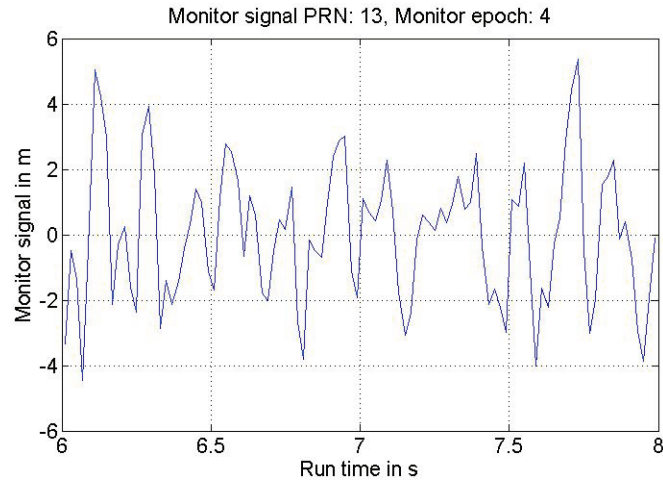


FIGURE 10 FDCC monitor signal for PRN 13 over epoch 4

3.2.2 | Strong Satellite

The C/A code signal from PRN 13 has 10-dB higher received power. Monitor results are shown over the same time interval. For the strong satellite signal, the sinusoidal behavior is less apparent, and the error amplitude is lower. This is pictured in Figure 9. The monitor signal selection used for screening is pictured in Figure 10. The monitor signal has not been adjusted for variance. The screening results for monitor epoch 4, which occurs from 6–8 seconds (runtime), are pictured in Figure 11.

PRN 13 has less severe self-interference error on the pseudorange measurement. As a result, a sinusoid is not detected on the strong signal. The code noise is significantly smaller, with $\sigma_{\text{code}} = 1.774$. The FDCC detector has a minimum detectable sinusoid amplitude $2A_{i,\min} = 6.162$ m in the measurement domain for the monitor signal created using unsmoothed measurements.

Self-interference must be detected if it grows to a significant error. Given the smaller error magnitude, self-interference is unlikely to create a significant error on the smoothed pseudorange measurement as shown in Figure 12. Based on the

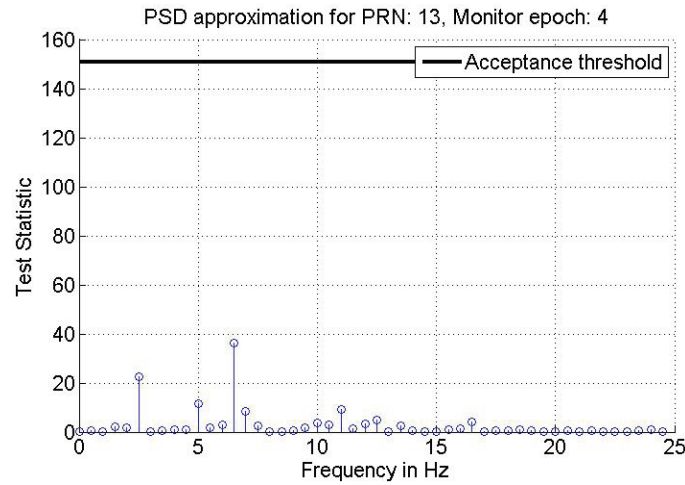


FIGURE 11 FDCC monitor signal spectrum for PRN 13 over epoch 4

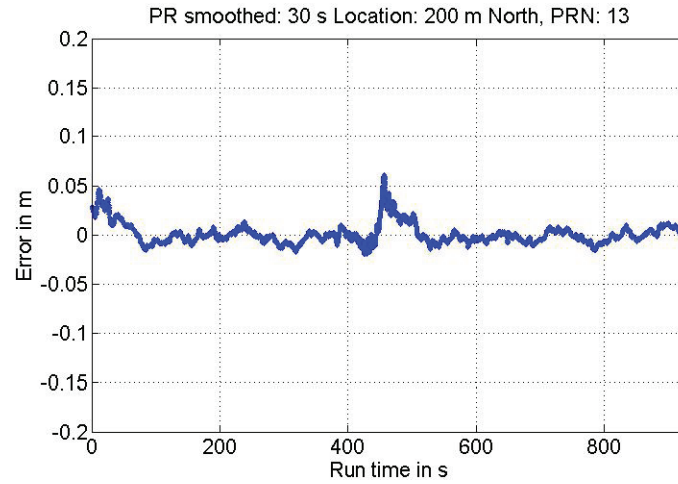


FIGURE 12 30-s smoothed CMC for PRN 13 over the duration of the simulated event

results, self-interference error is detected on the weak signal over 7-min before the maximum bias occurs on the smoothed pseudorange measurement. The goal of applying the detector is to screen all signals and detect when significant self-interference is present but flag the signals for removal based on the bias on the 30-s smoothed pseudorange measurement. The smoothed pseudorange results for the strong satellite were also formed using a correlator spacing of 0.083 chips. Adjusted for 0.1-chip correlator spacing, the maximum value becomes approximately 0.078 m at 456.5 s.

Accounting for the reduced correlator spacing, the maximum expected pseudorange error for PRN 3 is 4.928 m and for PRN 13 is 0.493 m. The maximum errors in the observed results (Figure 8 and Figure 12) are approximately 0.65 m and 0.065 m, respectively. The observed error does not reach the maximum expected pseudorange error due to the navigation data on the signals. The data bit values and relative alignment on the affected signals can cause energy from self-interference to cancel. As a result, the pseudorange error does not build to the maximum magnitude. The maximum can be reached, however, when the relative received signal power difference is larger than 10 dB due to flex power.

4 | BIAS-VALUE MONITOR

The feasibility of applying the Bias-Value monitor to detect self-interference was investigated in Belzer and van Graas (2019). The previous results are summarized in Section 1. In Belzer and van Graas (2019), unsmoothed pseudorange measurements were used to create the B-Value. These results also show the frequency modulation of the error. For the analysis, two receiver locations 200- and 400-m north of the stressful case of self-interference origin were used to observe the event. The self-interference event is described in Section 2.1. In current GBAS operations, the B-Value is resolved using smoothed measurements. To further evaluate the monitor, B-Values were generated using the 30-s smoothed CMC measurements. The results are given in Figure 13.

The B-Value monitor implemented with smoothing also responds to the self-interference event. In this plot and the previous results (Figure 2 and Figure 3), a hypothetical B-Value threshold value is marked by the dashed line. A B-Value threshold is given by the following expression (Dautermann et al., 2011):

$$B(i, j) > \frac{K_B \sigma_{pr, gnd, i}}{\sqrt{M-1}} \quad (22)$$

where K_B is a monitor false detection multiplier, and $\sigma_{pr, gnd}$ is the standard deviation of the smoothed pseudorange measurements. M is the number of reference receivers used to compute the monitor value (Dautermann et al., 2011). Based on this expression, a hypothetical B-Value threshold was derived. K_B was assigned a value of 5 and $\sigma_{pr, gnd}$ was assigned a value of 20 cm. This yields a B-Value threshold of 1 m.

Based on the example threshold, the monitor would detect self-interference on the pseudorange measurement for the weak satellite when implemented using unsmoothed measurements (Figure 2). For the observed results, the B-Value using unsmoothed measurements did not exceed the threshold for the strong satellite (Figure 3). However, after adjusting the results for a correlator spacing of 0.1 chips, it is expected that the monitor value would exceed the threshold for both the weak and strong satellite signals. For the weak satellite signal, the B-Value formed using unsmoothed measurements exceeds the threshold early, roughly 200-s into

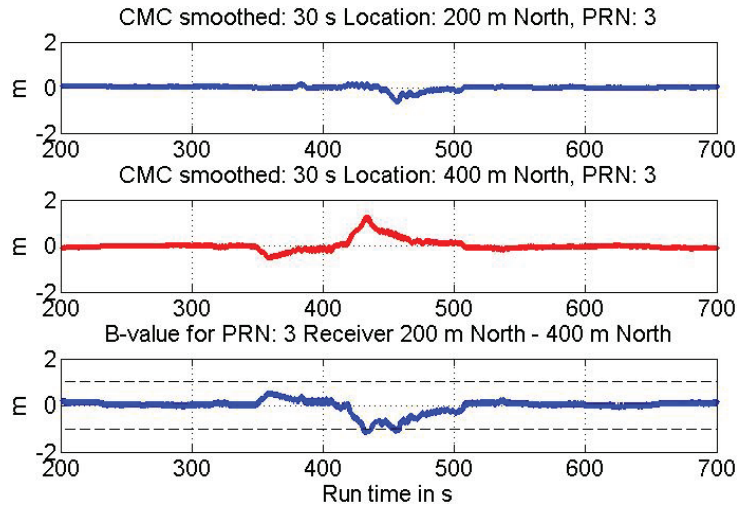


FIGURE 13 CMC measurements and bias value with smoothing for PRN 3

processing. In the case of the strong signal, the B-Value begins to approach the threshold 405.5-s into processing.

The B-Value also exceeds the threshold for the weak satellite when carrier smoothed pseudorange measurements with a 30-s time constant are used, as shown in Figure 13. For the weak satellite, the B-Value using smoothed measurements exceeds the threshold at approximately 432 s. In the case of the strong satellite, the B-Value using smoothed measurements has no clear detection or largest monitor response point. The B-Value monitor detects the error on the weak satellite signal before the worst error in the smoothed pseudorange measurements occurs (at 456.5 s).

5 | DETECTOR OPTIONS AND RECOMMENDATION

The B-Value monitor (using 30-s smoothed or unsmoothed pseudorange measurements) and the FDCC detector can detect self-interference on the pseudorange measurement. Additional detail on the unsmoothed pseudorange B-Value approach and the difference in the Doppler frequency projection for the receiver locations is included in Belzer and van Graas (2019). The B-Value monitor using unsmoothed measurements and the FDCC detector monitor signal both isolate the time-varying portion of the self-interference error on the pseudorange measurement. The B-Value monitor isolates it through geometry, while the FDCC monitor isolates it through signal frequency domain processing. The B-Value monitor uses at least two reference receivers, while the FDCC detector offers a single receiver solution. While the FDCC detector can be implemented using a single receiver, a two-receiver solution could offer more robust performance if one receiver experiences multipath. The FDCC detector is targeted for self-interference, while the B-Value monitor is sensitive to several anomalies, including reference receiver faults, multipath, and ionospheric gradients.

The B-Value monitor using unsmoothed measurements has the potential to detect the error. It detected the error on the weak satellite but did not exceed the threshold for the strong signal. It would likely detect self-interference error before it exceeds 1.6 m on the smoothed pseudorange measurement. The smoothed measurement approach detected the error on the weak satellite but may not offer rapid protection against a strong case of self-interference. Events caused by flex power or ghost satellites could cause severe error that may not be known ahead of time. If the value exceeds the threshold, it can flag a signal for removal from the solution, but it does not distinguish between self-interference and other bias-inducing errors.

The feasibility of detecting self-interference using the B-Value monitor was demonstrated using two receiver locations. A computer simulation was performed to determine if the monitor could be blinded using a two-receiver solution. A blind spot would occur if the Doppler crossover takes place at the same time for two receiver locations. The simulation uses two receivers positioned 200-m apart. A stationary receiver is positioned at the stressful case of self-interference event origin. A second receiver is placed 200-m east of the origin and rotated in a full circle counterclockwise. For each receiver configuration, the self-interference event is observed, and the Doppler crossover time observed by the mobile receiver is recorded. The results are pictured in Figure 14.

Figure 14 shows the Doppler crossover time for each rotating receiver configuration relative to the time it occurs for the stationary antenna. Based on the simulation, a two-receiver B-Value monitor solution is blinded to error caused

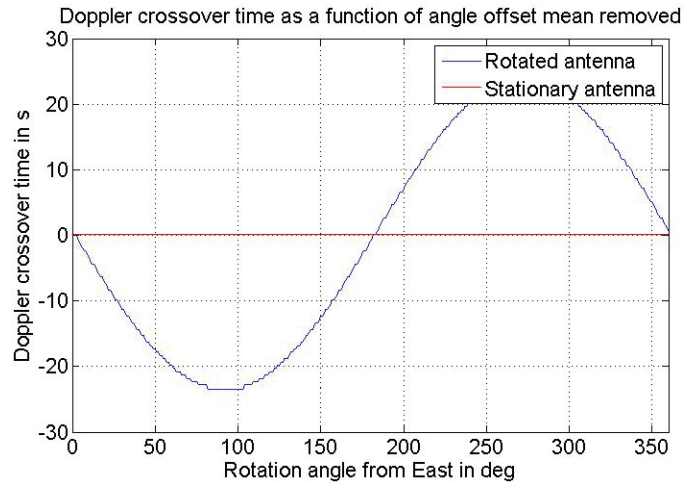


FIGURE 14 Doppler crossover observation times relative to stationary antenna crossover

by self-interference when the reference receivers are placed in approximately an east-west orientation. A solution using three reference receivers in a diverse geometry would likely not be blinded to self-interference but does impose siting constraints in terms of distance between receivers and geometry.

The FDCC detector isolates the error through signal processing techniques that respond differently to self-interference. Since the detector is not geometry dependent, it cannot experience a blind spot in the same way as the B-Value monitor. The novel approach also offers error separability because it detects based on the frequency modulation characteristic of self-interference. Detection based on frequency offers early detection with the potential to monitor the signal after self-interference has been identified. This allows for an adaptive approach based on the change in frequency over time. If the detected frequency trends toward zero, the pseudorange corrections can be used with confidence until the bias meets the error threshold. If the frequency increases, a bias may never build on the corrections. The targeted approach of the FDCC detector provides additional error context in the GAST-D environment. This research and Belzer and van Graas (2019) have demonstrated that multiple GBAS monitors respond to self-interference. If error caused by self-interference is misidentified, a satellite could be excluded from the solution longer than necessary. It is therefore important for the self-interference error to be detected before it impacts the other monitors.

The B-Value monitor and the FDCC detector operate on the target signal and screen each satellite signal. If either monitor is used, the GBAS solution will be guarded against self-interference on the weak and strong satellite signals in a self-interfering pair if the error on either signal grows to a significant bias. Since the monitors operate on the target signal, they do not require the interfering C/A code signal to be tracked. This makes them robust to self-interference error caused by flex power and ghost satellites.

Table 2 summarizes the applicability of the FDCC detector to the requirements and concerns for detecting self-interference in the GAST-D environment. The unsmoothed B-Value monitor also has the potential to detect the error with a timely response. However, a B-Value approach would require a minimum of three receivers. The B-Value monitor does not offer separation of self-interference from other bias-inducing errors. Implemented with smoothed measurements, it can detect self-interference but may not detect it within the required time to alert. The unsmoothed B-Value monitor and the FDCC detector have the potential to

TABLE 2
FDCC Detector Applicability Summary

Self-interference concerns	Requirement	FDCC Detector applicability
Pseudorange error bound	1.6 [m] with 10^{-9} probability	Yes
Time to alert	2 [s]	Yes
Reduced smoothing time constant	30 [s]	Yes
Ghost satellites	No need to track all satellites that could introduce self-interference	Yes
Flex power	Operate in the presence of large power differences between satellites	Yes

be applied to detect self-interference on the pseudorange measurement in the GAST-D environment. Both approaches require minimal changes to the GBAS ground system. The B-Value approach would require reference receivers to have a diverse geometry. The FDCC detector can be used to screen all signals from all reference receivers.

Frequency modulation of pseudorange error is unique to self-interference and multipath. During a (non-multipath) self-interference event, all reference receivers will detect sinusoidal error with a similar frequency. Errors caused by multipath will be observed by only one receiver at a time and are limited through antenna design and antenna siting. Both errors are constellation dependent, but multipath is caused by an antenna's local environment.

To apply the FDCC monitor to screen for self-interference in the GBAS environment, some considerations remain. The effects of signal windowing on the DFT results should be considered. Additionally, the effects of the relative navigation data bit values on the two self-interfering signals on the detector should be evaluated. Additional future work includes evaluating the performance of the monitor over multi-day simulations using real-world conditions. These would include atmospheric effects and varying navigation data bit values.

The CCD and DSIGMA monitors were also found to respond to self-interference (Belzer & van Graas, 2019). The 30-s smoothed pseudorange results presented offer additional insight into the performance of the monitors. The maximum error on the smoothed pseudorange measurement for PRN 3 (Figure 8) over the duration of the event was found to be approximately 0.65 m. Based on these results, it is expected that the CCD monitor would detect a self-interference error of 1.6 m on the smoothed pseudorange measurement. The DSIGMA monitor would also likely exceed the threshold for an error of 1.6 m. However, these monitors rely on smoothed pseudorange measurements. This makes them less attractive options for detecting the error within the required time to alert. Since the CCD and DSIGMA monitors were found sensitive to self-interference, they could misidentify the error under their primary application within GBAS. Use of a self-interference-specific detector could be applied to mitigate error misidentification by other monitors.

6 | CONCLUSION

This work investigated the ability of monitors to detect self-interference error on the pseudorange measurement in the GBAS GAST-D environment. It serves as a first step in developing a self-interference monitoring strategy. Monitors are

evaluated for their performance using a stressful case of self-interference. This case is severe based on the Doppler geometry and crossover event. During the event, self-interference conditions occur for a duration greater than 12 seconds. The ability of the CCD monitor, DSIGMA, and B-Value monitor to detect self-interference is summarized. This paper focuses on the feasibility of applying the B-Value monitor and presents the FDCC detector. The FDCC detector works by screening the frequency spectrum of the monitor signal over a duration of 2 s.

The B-Value monitor and the FDCC detector are viable options for detection in the GAST-D environment. The B-Value monitor has the potential to detect self-interference when implemented using unsmoothed pseudorange measurements. A two-receiver solution was found to experience a blind spot to self-interference. A minimum of three receivers with a diverse geometry are required to unblind the monitor.

The FDCC detector offers targeted detection using a single receiver. Specific detection of self-interference provides error separability and offers potential for increased measurement availability. The FDCC detector detected error on the pseudorange measurement of the weak satellite over 7-min before the maximum bias on the smoothed pseudorange measurement occurred. Early detection would allow an error projection or monitoring after detection. The pseudorange measurement could be excluded before the error exceeds the bound. Both the B-Value monitor and the FDCC detector screen each satellite signal individually and are applicable to detecting self-interference from flex power and ghost satellites.

The CCD monitor, DSIGMA, and B-Value monitor using smoothed pseudorange measurements were found to respond to self-interference. These monitors may misidentify error caused by self-interference in their primary application. A targeted solution offering self-interference error separability, such as the FDCC monitor, has potential for managing error misidentification of other monitors and can increase contextual awareness of errors in the GBAS environment.

REFERENCES

- Belzer, J. A., & van Graas, F. (2019). GPS C/A code self-interference: error detection using existing GBAS monitors. *Proc. of the ION 2019 Pacific PNT Meeting*, Honolulu, HI, 997–1012. <https://doi.org/10.33012/2019.16781>
- Braasch, M. S. (1996). Multipath effects. In J. J. Spilker Jr., P. Axelrad, B. W. Parkinson, & P. Enge (Eds.), *Global Positioning System: theory and applications* (Vol. 1, pp. 547–568). American Institute of Aeronautics and Astronautics, Inc. <https://doi.org/10.2514/5.9781600866388.0547.0568>
- Brown, R. G., & Chin, G. Y. (1997). *GPS RAIM: calculation of threshold and protection radius using chi-square methods; a geometric approach*. Radio Technical Commission for Aeronautics.
- Dautermann, T., Felux, M., & Grosch, A. (2011). Approach service Type D evaluation of the DLR GBAS testbed. *GPS Solutions*, 16, 375–387. <https://doi.org/10.1007/s10291-011-0239-3>
- Federal Aviation Administration (FAA). (n.d.). *Satellite navigation - GBAS - how it works*. Federal Aviation Administration/US Department of Transportation. https://www.faa.gov/about/office_org/headquarters_offices/ato/service_units/techops/navservices/gnss/laas/howitworks
- Groth, E. J. (1975). Probability distributions related to power spectra. *The Astrophysical Journal Supplement Series*, 286(29), 285–302. <https://doi.org/10.1086/190343>
- Gunawardena, S. (2013). A universal GNSS software receiver MATLAB® toolbox for education and research. *Proc. of the 26th International Technical Meeting of the Satellite Division of the Institute of Navigation (ION GNSS+ 2013)*, Nashville, TN, 1560–1576. <https://www.ion.org/publications/abstract.cfm?articleID=11230>
- Hatch, R. (1982). The synergism of GPS code and carrier measurements. *Proc. of the 3rd International Geodetic Symposium on Satellite Doppler Positioning*, 1213–1232.
- Houston, T., Liu, F., & Brenner, M. (2011). Real-time detection of cross-correlation for a precision approach ground based augmentation system. *Proc. of the 24th International Technical Meeting of the Satellite Division of the Institute of Navigation (ION GNSS 2011)*, Portland, OR, 3012–3025. <http://www.ion.org/publications/abstract.cfm?jp=p&articleID=9858>
- ICAO NSP/3. (2016). *Conceptual framework for the proposal for GBAS to support CAT III operations* (Flimsy 10; pp. 1–76). International Civil Aviation Organization.

- MathWorks. (n.d.). *MATLAB - MathWorks*. MathWorks. <https://www.mathworks.com/products/matlab.html>
- Papoulis, A. (1965). *Probability, random variables, and stochastic processes*. McGraw-Hill Book Company.
- RTCA SC-159. (2008). *GNSS based precision approach local area augmentation system (LAAS) – signal-in-space interface control document* [Interface Control Document No. DO246D]. RTCA, Inc. <https://standards.globalspec.com/std/1201621/rtca-do-246>
- RTCA SC-159. (2017). *Minimum operational performance standards for GPS local area augmentation system airborne equipment* [Minimum Operational Performance Standards RTCA DO-253D]. RTCA, Inc. <https://standards.globalspec.com/std/10168693/RTCA%20DO-253>
- Soloviev, A., Gunawardena, S., & van Graas, F. (2005). Development of high performance high update rate reference GPS receiver. *Proc. of the 18th International Technical Meeting of the Satellite Division of the Institute of Navigation (ION GNSS 2005)*, Long Beach, CA, 1621–1631. <https://www.ion.org/publications/abstract.cfm?articleID=6360>
- Spilker, J. J. (1978). Signal structure and performance characteristics (space segment), *NAVIGATION*, 25(2), 121–146. <https://www.ion.org/publications/abstract.cfm?articleID=100680>
- Steigenberger, P., Thörlert, S., & Montenbruck, O. (2019). Flex power on GPS Block IIR-M and IIF. *GPS Solutions*, 23(8). <https://doi.org/10.1007/s10291-018-0797-8>
- Van Dierendonck, A. J., Erlandson, R., McGraw, G., & Coker, R. (2002). Determination of C/A code self-interference using cross-correlation simulations and receiver bench tests. *Proc. of the 15th International Technical Meeting of the Satellite Division of the Institute of Navigation (ION GPS 2002)*, Portland, OR, 630–642. <https://www.ion.org/publications/abstract.cfm?articleID=2065>
- van Nee, R. D. J. (1992). GPS multipath and satellite interference. *Proc. of the 48th Annual Meeting of the Institute of Navigation*, Dayton, OH, 167–178. <https://www.ion.org/publications/abstract.cfm?articleID=4768>
- Vidakovic, B. (2011). *Statistics for bioengineering sciences: with MATLAB and WinBUGS support*. Springer. <https://doi.org/10.1007/978-1-4614-0394-4>
- Zhu, Z., & van Graas, F. (2005). Operational considerations for C/A code tracking errors due to cross correlation. *Proc. of the 18th International Technical Meeting of the Satellite Division of the Institute of Navigation (ION GNSS 2005)*, Long Beach, CA, 1255–1262. <https://www.ion.org/publications/abstract.cfm?articleID=6322>
- Zhu, Z., & van Graas, F. (2011). C/A code cross correlation error with carrier smoothing - the choice of time constant: 30 s vs. 100 s. *Proc. of the 2011 International Technical Meeting of the Satellite Division of the Institute of Navigation*, San Diego, CA, 464–472. <http://www.ion.org/publications/abstract.cfm?jp=p&articleID=9490>
- Zhu, Z., & van Graas, F. (2014). Implications of C/A code cross correlation on GPS and GBAS. *Proc. of the IEEE/ION PLANS 2014*, Monterey, CA, 282–293. <https://www.ion.org/publications/abstract.cfm?articleID=11645>

How to cite this article: Belzer, J., & van Graas, F. (2023). Detection of GPS C/A code self-interference: monitor overview and applicability. *NAVIGATION*, 70(1). <https://doi.org/10.33012/navi.559>